IEEE Access
Multidisciplinary | Rapid Review | Open Access Journal

Received March 31, 2021, accepted April 9, 2021, date of publication April 14, 2021, date of current version April 22, 2021.

Digital Object Identifier 10.1109/ACCESS.2021.3072844

Influence of Salient Effect on Air-Gap Flux Density Distribution of Interior Permanent-Magnet Synchronous Machines

JIAKUAN XIA, ZEXING LI, ZIXUAN ZHANG, AND ZHIYAN GUO
School of Electrical Engineering, Shenyang University of Technology, Shenyang 110000, China
Corresponding author: Zexing Li (lzxsut@qq.com)

This work was supported in part by the Natural Science Foundation of China under Grant 52077142.

ABSTRACT Interior permanent magnet synchronous machines (IPMSMs) are widely used in electric vehicles due to their high power density, high efficiency, and wide speed range. Compared with surface-mounted PMSMs, the salient effect of IPMSMs causes a significant difference between quadrature-axis and direct-axis flux paths, which can increase the harmonic components of the air-gap field and affect the operation of the machine. Herein, taking a 6-poles 36-slots PMSM as an example, this paper analyzes the influence of salient effect on the air-gap flux density. Based on salient effect function, the analytical model of air-gap flux density considering the salient effect is established, and the influence of the salient effect on the spatial-temporal distribution characteristics of air-gap flux density excited by permanent magnets and armature reaction are derived, which are verified by the finite element method (FEM). Both simulation and experiment results of the prototype show good agreement, and the sources of salient effect are found with finite element model and equivalent magnetic circuit. Further, different current excitations are applied to analyze the influence of the salient effect on different magnetic fields. The results show that the salient effect has a more significant influence on the direct-axis armature reaction magnetic field, which increases the harmonics components with the temporal orders of $3k_a$ ($k_a = 1, 2, 3 \ldots$).

INDEX TERMS IPMSMs, salient effect, quadrature-axis and direct-axis flux paths, spatial-temporal distribution, equivalent magnetic circuit, FEM.

I. INTRODUCTION

THE interior permanent magnet synchronous machines (IPMSMs) are widely used in electric vehicles due to the significant advantages which can be yielded, such as high efficiency, high power density, and wide speed range [1], [2]. These features contribute to the performance of the power system of electric vehicles [3], [4].

The air-gap magnetic field is the energy conversion medium, and its spatial-temporal distribution characteristics directly affect the running performance of the machine [5]–[7]. To date, the research on the air-gap magnetic field of surface-mounted permanent magnet synchronous machines (SPMSMs) has been fully developed, due to their regular permanent magnet (PM) layout and simple magnetic circuit [8]–[13].

Compared with SPMSMs, the salient effect of IPMSMs, caused by PMs buried in the rotor core, results in a significant difference between quadrature-axis and direct-axis flux paths, which can increase the harmonic components of air-gap field and affect the operation of the machine [14]–[17]. In [18], a simple magnetic reluctance network, considering the geometry of the machine and the material characteristics, was used to analyze the effect of stator slotting on the magnetic field distribution of salient pole PMSMs. In [19], a new armature reaction magnetic field model, considering the effect of the embedded magnet in the rotor, was proposed, which can be used to evaluate various machine performances, such as inductance, stator core losses, and magnet eddy current losses. In [20], equivalent magnetic circuit method (MCM), conformal mapping and concentration flux were combined to analyze and design a multi-layered and multi-segmented IPMSM. In [21], a method to model the saturation level and the relative permeability at different regions of the rotor iron was proposed, based on the rotor geometry and the nonlinear B-H curve of the iron core, and the problem of inaccurate calculation caused by nonlinear saturated rotor was solved. In [22],

The associate editor coordinating the review of this manuscript and approving it for publication was Shihong Ding.

an extended analytical method, based on the conformal mapping technique, was used to predict the open-circuit air-gap field distribution in an IPMSM equipped with multilayer PMs. In [23], based on the complex relative permeance, accounting for the slotting effect, the radial and tangential air-gap flux densities were calculated rapidly.

Remarkably, air-gap magnetic field of IPMSMs is more complex than that of SPMSMs based on the above literature, which is mainly caused by salient effect due to PMs buried in the rotor core [24]. However, the research on the influence of salient effect on air-gap magnetic field, as of writing, not yet been fully developed. The air gap permeance and the spatial-temporal distribution of air-gap flux density can be changed greatly due to the salient effect, which can result in significant vibration and additional losses, affecting the operation of the IPMSMs [25]. These significant variations caused by salient effect are not considered in conventional analysis in literature. Therefore, there is an urgent need to develop an analysis method to research the influence and sources of the salient effect on the air-gap flux density distribution of IPMSM, which can be used as the basis for the research of loss and vibration.

Taking a 6-poles 36-slots IPMSM as an example, this paper aims to analyze the influence of salient effect on the air-gap flux density. In Section 2, the basic parameters of the prototype are given, and the excitation setting under different magnetic fields is described. In Section 3, the analytical model of air-gap flux density considering saient effect is derived, based the salient effect function, and the spatial-temporal distribution characteristics under permanent magnetic field (PMF) and armature reaction magnetic field (ARMF) are investigated, respectively. In Section 4, the air-gap flux density is calculated with finite element method (FEM). Finally, the prototype experiment is carried out to verify the finite element model and the sources of the salient effect are found. The obtained conclusions can serve as a valuable reference for the analysis of the multi-physical field of IPMSMs.

II. PROPOSED MODELING OF IPMSM

A. SPECIFICATIONS OF THE PROTOTYPE

The cross-sectional view of the prototype investigated in this paper is shown Fig. 1. It should be emphasized that the salient effect is mainly caused by the buried PMs, flux barriers and magnetic bridges [18], [23], [24].

The basic parameters of the IPMSM are listed in Table 1. The machine is a 6-poles 36-slots IPMSM with a rated power of 1.9 kW, and the rated current is 22.8 A.

TABLE 1. Basic parameters of the 1.9 kW PMISG.

Specifications	Values
Rated power, kW	1.9
Rated speed, r/min	1500
Rated current, A	22.8
Number of poles and slots	6/36

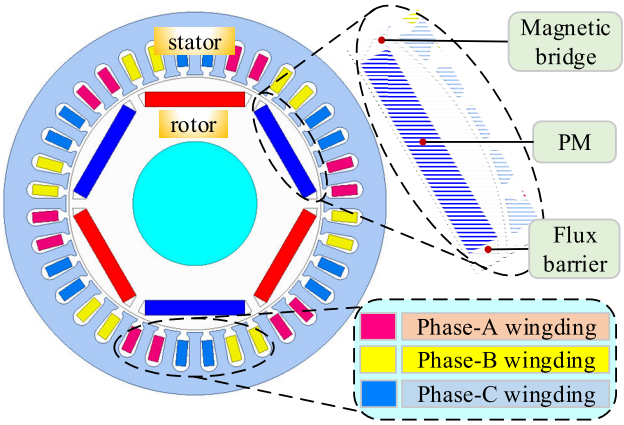

FIGURE 1. The cross-section diagram of the protype.

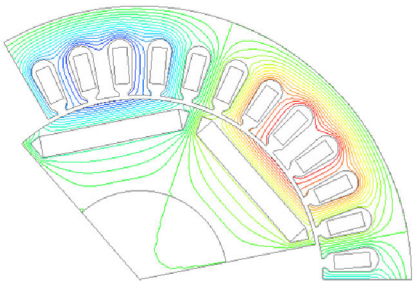

FIGURE 2. The quadrature-axis flux path.

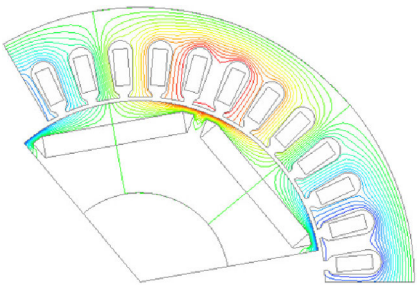

FIGURE 3. The direct-axis flux path.

B. EXCITATION SETTING OF THE PROTOTYPE

Fig. 2 and Fig. 3 show the quadrature-axis flux path and direct-axis flux path respectively, when the PMs are replaced by using a non-magnetic source with the same magnetic permeability. It can be seen that the path and phase between the two flux paths are significantly different. Therefore, it is very necessary to decompose the ARMF into quadrature-axis ARMF and direct-axis ARMF, so as to further study the influence of the salient effect on the two.

Based on the principle of equivalent magneto motive force (MMF), this paper decomposes the armature reaction by adjusting the three-phase current.

The corresponding three-phase current only considering quadrature-axis ARMF can be given as

$$\begin{bmatrix} i_{Aq} \\ i_{Bq} \\ i_{Cq} \end{bmatrix} = \sqrt{\frac{2}{3}} \begin{bmatrix} \cos\theta & -\sin\theta \\ \cos(\theta - \frac{2}{3}\pi) & -\sin(\theta - \frac{2}{3}\pi) \\ \cos(\theta - \frac{4}{3}\pi) & -\sin(\theta - \frac{4}{3}\pi) \end{bmatrix} \begin{bmatrix} 0 \\ i_Q \end{bmatrix} \quad (1)$$

where θ is the angular position, and i_Q is equivalent quadrature-axis current, the effective value range is between zero and the square root of one and half of rated current.

The corresponding three-phase current only considering direct-axis ARMF can be given as

$$\begin{bmatrix} i_{Ad} \\ i_{Bd} \\ i_{Cd} \end{bmatrix} = \sqrt{\frac{2}{3}} \begin{bmatrix} \cos\theta & -\sin\theta \\ \cos(\theta - \frac{2}{3}\pi) & -\sin(\theta - \frac{2}{3}\pi) \\ \cos(\theta - \frac{4}{3}\pi) & -\sin(\theta - \frac{4}{3}\pi) \end{bmatrix} \begin{bmatrix} i_D \\ 0 \end{bmatrix} \quad (2)$$

where i_D is equivalent direct-axis current, the effective value range is between zero and the square root of one and half of rated current.

III. ANALYSIS OF AIR-GAP MAGNETIC FIELD

A. ANALYTICAL MODEL OF AIR-GAP PERMEANCE

When the salient effect is considered, the air gap permeance function will change. The rotor salient structure can be approximately equivalent to the rotor slot effect. With the consideration of the slot effect and the salient effect, the equivalent air gap permeance can be expressed as [23], [26]

$$\Lambda_\delta(\theta, t) = \Lambda_0 \lambda_1(\theta) \lambda_2(\theta, t) \quad (3)$$

where t is the time, and Λ_0 is average air gap permeance. $\lambda_1(\theta)$ and $\lambda_2(\theta, t)$ are the relative permeance function of the slot effect and salient effect, respectively, which can be written as

$$\begin{cases} \lambda_1(\theta) = 1 + \sum_{k_Z} A_{k_Z} \cos(k_Z Z\theta) \ (k_Z = 1, 2, 3 \ldots) \\ \lambda_2(\theta, t) = 1 + \sum_{k_S} A_{k_S} \cos 2k_S(p\theta - \omega t) \ (k_S = 1, 2, 3 \ldots) \end{cases} \quad (4)$$

where A_{k_Z} is the magnitude of the $k_Z - th$ harmonic permeance, and Z is the number of slots. A_{k_S} is the magnitude of the $k_S - th$ harmonic permeance, ω is the angular frequency of current source, and p is the number of pole pairs.

Substituting (4) into (3), the equivalent air gap permeance can be expressed as

$$\begin{aligned} \Lambda_\delta(\theta, t) &= \Lambda_0 \lambda_1(\theta) \lambda_2(\theta, t) \\ &= \Lambda_0 + \sum_{k_Z} \Lambda_{k_Z} \cos(k_Z Z\theta) \\ &\quad + \sum_{k_S} \Lambda_{k_S} \cos 2k_S(p\theta - \omega t) \\ &\quad + \frac{1}{2} \sum_{k_Z} \sum_{k_S} \Lambda_{k_Z} \Lambda_{k_S} \cos \begin{bmatrix} (k_Z Z + 2k_S p)\theta \\ \pm 2k_S \omega t \end{bmatrix} \end{aligned} \quad (5)$$

The sources and spatial-temporal orders of the equivalent air gap permeance can be found from (5), as shown in Table 2. It can be seen from Table 2 that the sources of the equivalent air gap permeance mainly include four terms, i.e., the average permeance, the stator slot effect, the salient effect, and the interaction between the stator slot effect and the salient effect.

TABLE 2. Sources and spatial-temporal orders of air gap permeance.

Sources	Spatial order	Temporal order
Average permeance	/	/
Stator slot effect	$k_Z Z$	/
Salient effect	$2k_S p$	$2k_S$
Interaction between stator slot effect and salient effect	$k_Z Z + 2k_S p$	$2k_S$

TABLE 3. Sources and spatial-temporal orders of PMF.

Sources	Spatial order	Temporal order
Interaction between PMMF and average permeance	$\nu_R p$	ν_R
Interaction between PMMF and stator slot effect	$\nu_R p \pm k_Z Z$	ν_R
Interaction between PMMF and salient effect	$(\nu_R \pm 2k_S)p$	$\nu_R \pm 2k_S$
Interaction among PMMF, stator slot effect and salient effect	$(\nu_R \pm 2k_S)p \pm k_Z Z$	$\nu_R \pm 2k_S$

When the salient effect is considered, the air gap permeance is the function of position and time, and increases the harmonic permeance with the temporal orders of $2k_S$ and the spatial orders of $2k_S p$ and $k_Z Z + 2k_S p$, respectively.

B. ANALYTICAL MODEL OF PMF

The MMF generated by the PMs is expressed as [27], [28]

$$F_R = \sum_{\nu_R} F_{Rm}^{\nu_R} \cos \nu_R(p\theta - \omega t) \quad (6)$$

where $F_{Rm}^{\nu_R}$ is the amplitude of the $\nu_R - th$ harmonic of MMF, and ν_R is the harmonic order of MMF generated by PMs, the value of which is $2k_R - 1 (k_R = 1, 2, 3 \ldots)$.

Multiplying (6) and (5), the air-gap flux density generated by PMs can be written as

$$\begin{aligned} B_{R\delta} &= F_R \Lambda_\delta(\theta, t) \\ &= \sum_{\nu_R} \Lambda_0 F_{Rm}^{\nu_R} \cos \nu_R(p\theta - \omega t) \\ &\quad + \frac{1}{2} \sum_{\nu_R} \sum_{k_Z} F_{Rm}^{\nu_R} \Lambda_{k_Z} \cos[(\nu_R p \pm k_Z Z)\theta - \nu_R \omega t] \\ &\quad + \frac{1}{2} \sum_{\nu_R} \sum_{k_S} F_{Rm}^{\nu_R} \Lambda_{k_S} \\ &\quad \times \cos[(\nu_R \pm 2k_S)p\theta - (\nu_R \pm 2k_S)\omega t] \\ &\quad + \frac{1}{4} \sum_{\nu_R} \sum_{k_Z} \sum_{k_S} F_{Rm}^{\nu_R} \Lambda_{k_Z} \Lambda_{k_S} \\ &\quad \times \cos \begin{Bmatrix} [(\nu_R \pm 2k_S)p \pm k_Z Z]\theta \\ -(\nu_R \pm 2k_S)\omega t \end{Bmatrix} \end{aligned} \quad (7)$$

According to (7), the sources and spatial-temporal orders of the PMF can be obtained as shown in Table 3. It can be found from Table 3 that the sources of the PMF mainly consists of four terms, i.e., the interaction between the permanent MMF (PMMF) and average permeance, the interaction between the PMMF and the stator slot effect, the interaction between the PMMF and the salient effect, and the

TABLE 4. Sources and spatial-temporal orders of ARMF.

Sources	Spatial order	Temporal order
Interaction between ARMMF and average permeance	$v_S p$	μ
Interaction between ARMMF and stator slot effect	$v_S p \pm k_Z Z$	μ
Interaction between ARMMF and salient effect	$(v_S \pm 2k_S)p$	$\mu \pm 2k_S$
Interaction among ARMMF, stator slot effect and salient effect	$(v_S \pm 2k_S)p \pm k_Z Z$	$\mu \pm 2k_S$

interaction among the PMMF, the stator slot effect, and the salient effect. With the consideration of the salient effect, the spatial-temporal orders of the new components of the air-gap flux density coincides with the original components. Therefore, the salient effect mainly changes the amplitudes of the original air-gap flux field components under PMF.

C. ANALYTICAL MODEL OF ARMF

The MMF excited by the three-phase symmetrical current in the stator windings is expressed as [29]

$$F_S = \sum_{\mu} \sum_{v_S} F_{Sm}^{\mu, v_S} \cos(v_S p\theta - \mu\omega t + \varphi^{\mu, v_S}) \tag{8}$$

where F_{Sm}^{μ, v_S} and φ^{μ, v_S} are the amplitude and initial phase angle of $v_S - th$ harmonic components of armature reaction MMF created by μ-th time current, respectively. v_S is the harmonic order of armature reaction MMF, and μ is the time current harmonic order, the value of which can be given as

$$\mu = 6k_S \pm 1 \quad (k_S = 0, 1, 2 \ldots) \tag{9}$$

Multiplying (8) and (5), the air-gap flux density generated by direct-axis armature reaction can be written as

$$\begin{aligned} B_{S\delta} &= F_S \Lambda_\delta(\theta, t) \\ &= \sum_{\mu} \sum_{v_S} \Lambda_0 F_{Sm}^{\mu, v_S} \cos(v_S p\theta - \mu\omega t + \varphi^{\mu, v_S}) \\ &\quad + \frac{1}{2} \sum_{\mu} \sum_{v_S} \sum_{k_Z} F_{Sm}^{\mu, v_S} \Lambda_{k_Z} \\ &\quad \times \cos[(v_S p \pm k_Z Z)\theta - \mu\omega t + \varphi^{\mu, v_S}] \\ &\quad + \frac{1}{2} \sum_{\mu} \sum_{v_S} \sum_{k_S} F_{Sm}^{\mu, v_S} \Lambda_{k_S} \\ &\quad \times \cos \begin{bmatrix} (v_S \pm 2k_S)p\theta + \\ (\mu \pm 2k_S)\omega t + \varphi^{\mu, v_S} \end{bmatrix} \\ &\quad + \frac{1}{4} \sum_{\mu} \sum_{v_S} \sum_{k_Z} \sum_{k_S} F_{Sm}^{\mu, v_S} \Lambda_{k_Z} \Lambda_{k_S} \\ &\quad \times \cos \begin{Bmatrix} [(v_S \pm 2k_S)p \pm k_Z Z]\theta \\ -(\mu \pm 2k_S)\omega t + \varphi^{\mu, v_S} \end{Bmatrix} \end{aligned} \tag{10}$$

According to (10), the sources and spatial-temporal orders of the ARMF can be obtained as shown in Table 4. It can be found from Table 4 that the sources of the ARMF mainly consists of four terms, i.e., the interaction between the armature reaction MMF (ARMMF) and average permeance, the interaction between the ARMMF and the stator slot effect, the interaction between the ARMMF and the salient effect, and the interaction among the ARMMF, the stator slot effect, and the salient effect. Considering the salient effect, the increasing harmonic components with the temporal orders of $\mu \pm 2k_S$ and the spatial orders of $(v_R \pm 2k_S)p$ and $(v_R \pm 2k_S)p + k_Z$ respectively, are different from the original components, which results in the additional harmonics with the temporal orders of $3k_a$ ($k_a = 1, 2, 3 \ldots$). In addition, the amplitudes of its various harmonics are also changed.

IV. CALCULATION OF AIR-GAP FLUX DENSITY BY FEM

A. CALCULATION OF PMF WITH FEM

Fig. 4 shows the curve and its corresponding 2-D Fast Fourier transform (FFT) result of PMF. It can be seen from Fig. 4 (b) that spatial orders and temporal orders of the PMF are $v_R p$ (3, 6, 9 ...) and v_R (1, 3, 5, 7 ...), respectively, which are coincident with the Table 3, thus the salient effect mainly changes the amplitudes of the original air-gap magnetic field components under PMF.

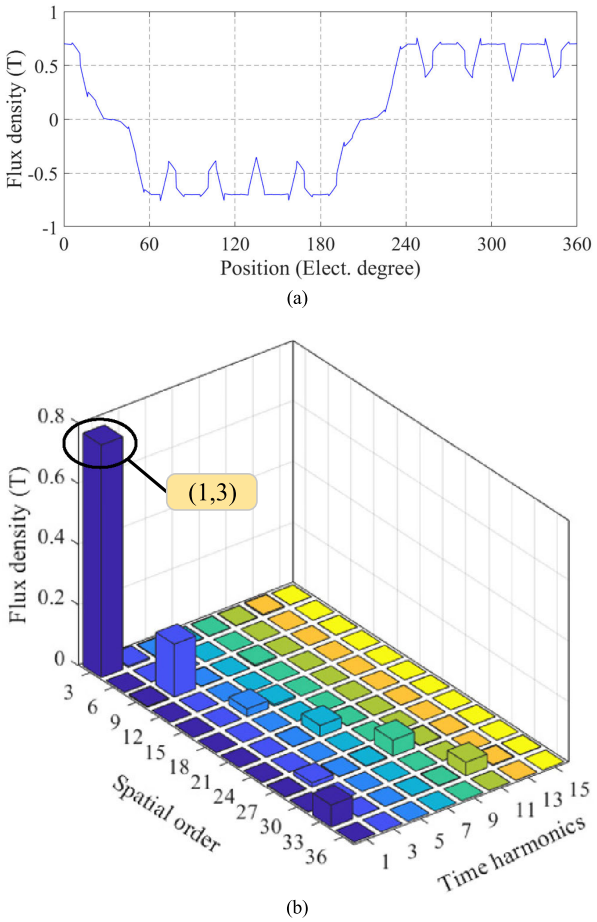

FIGURE 4. The air-gap flux density and its 2-D FFT result under PMF. (a) Flux density curve, (b) 2-D FFT result.

B. CALCULATION OF ARMF WITH FEM

Fig. 5 shows the curve and its corresponding 2-D FFT result of ARMF, which contains the quadrature-axis and direct-axis

components in the case of PMs being replaced with a non-magnetic material. It can be seen from Fig. 5 (b) that spatial orders and temporal orders of the ARMF are v_{RP} (3, 6, 9 …) and $\mu \pm 2k_S$ (1, 3, 5, 7 …), respectively, which are different from the Table 4. Considering the salient effect, the air-gap flux density increases the harmonic components with the temporal orders of $3k_a$ ($k_a = 1, 2, 3\ldots$), and the amplitudes of its various harmonics are also changed.

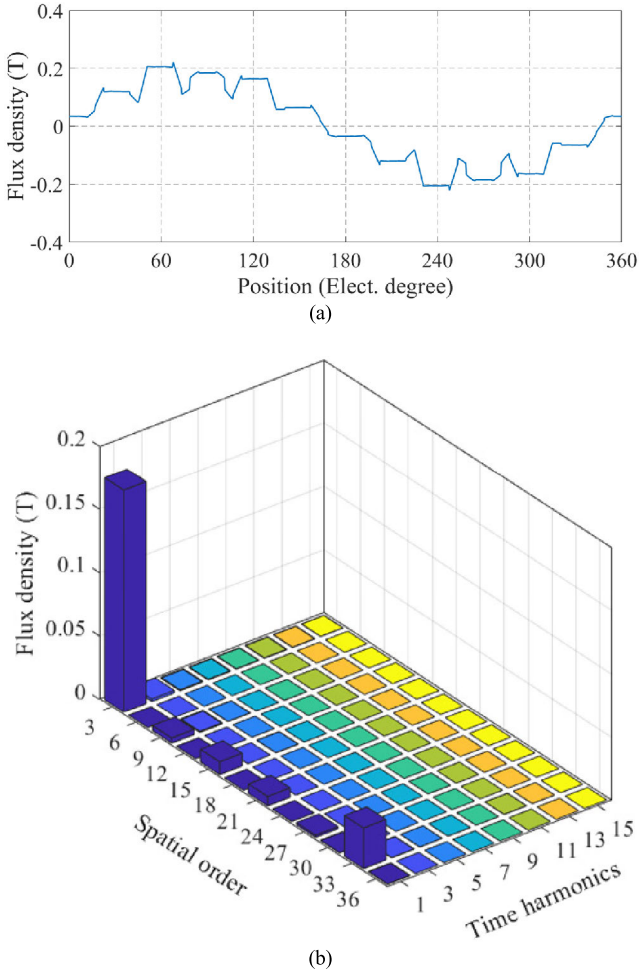

(a)

(b)

FIGURE 5. The air-gap flux density and its 2-D FFT result under ARMF. (a) Flux density curve, (b) 2-D FFT result.

V. EXPERIMENT AND DISCUSSION

In this section, the finite element model of 1.9kW IPMSM is first experimentally confirmed in no-load and load conditions. Then, the sources of the salient effect under different magnetic fields are studied, based on the proven model. After that, different quadrature-axis and direct-axis currents are input to the excitation to further study the influence of the salient effect on the air-gap magnetic field in the different conditions.

A. VERIFICATION OF FINITE ELEMENT MODEL

In order to verify the accuracy of the finite element model, the experiment platform of the prototype is set up, as shown

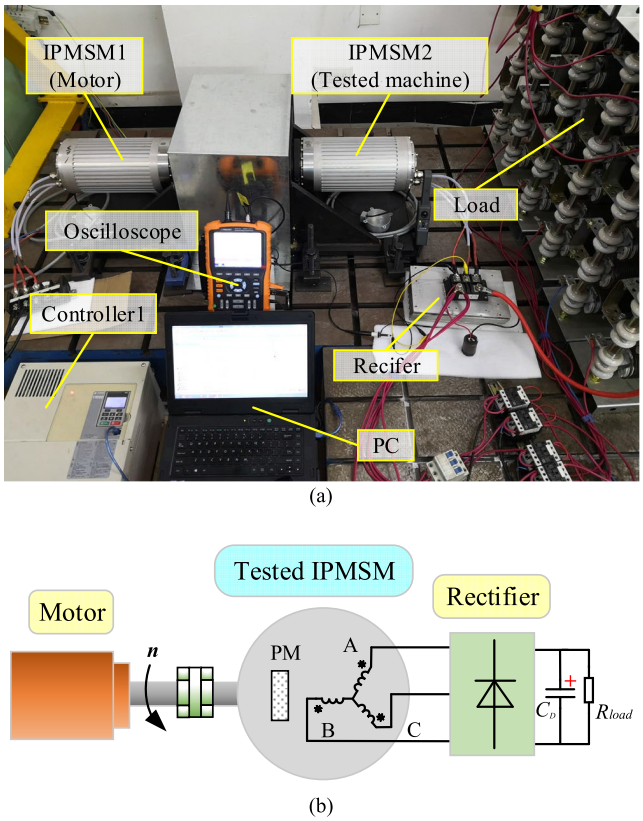

(a)

(b)

FIGURE 6. The Experimental set-up of the prototype. (a) Experimental system, (b) Schematic diagram.

in Fig. 6. The IPMSM1 runs as a motor, and the IPMSM2 runs a generator, as the tested prototype.

Under no-load condition, the winding is disconnected from the external circuit, and the oscilloscope is used to record the no-load line back EMF of the prototype. Under load condition, the winding is connected with the external circuit, and the line voltage and phase current are obtained with the oscilloscope. The measured results are as shown in Fig. 7 (a), and the corresponding effective values of which are 53.01 V, 52.59 V and 22.66 A, respectively. The simulation results are shown in Fig. 7 (b), which are consistent with the measured results.

B. SOURCES OF SALIENT EFFECT UNDER DIFFERENT MAGNETIC FIELDS

(i) Fig. 8 shows the magnetic field line diagram of the prototype under no-load condition, and the air-gap magnetic field is only excited by PMs. Ignoring the leakage magnetic field between poles, the main magnetic field passes through PMs, rotor core, air gap and stator core. Fig. 9 shows the magnetic density map of the prototype under no-load condition. The result shows that only the inter-pole region with severe magnetic leakage is saturated, and the main magnetic path does not appear to be saturated.

Ignoring the permeance of the cores the main magnetic circuit, the model of equivalent magnetic circuit under no-load condition is shown in Fig. 10. The PM is equivalent to a

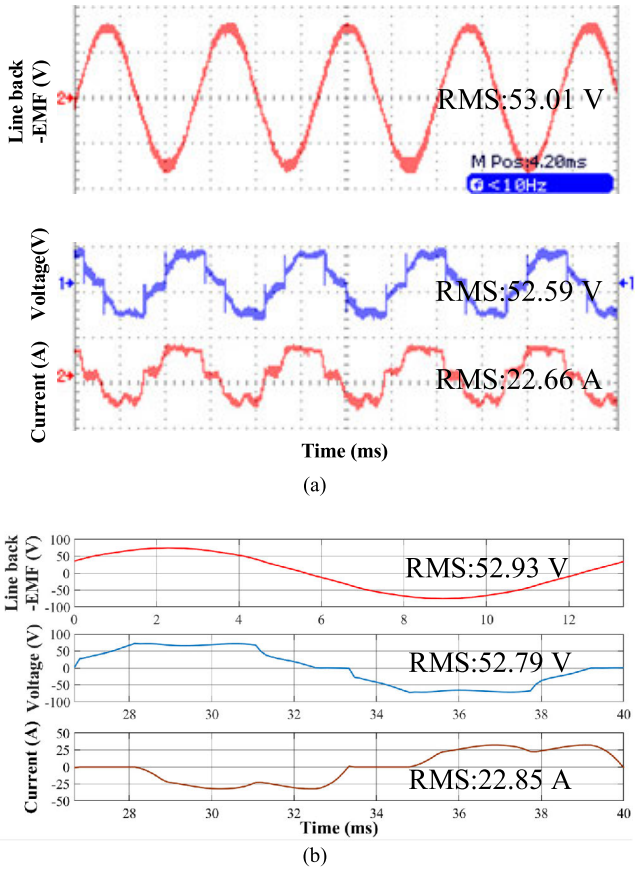

FIGURE 7. The experiment and simulation results. (a) Experimental results, (b) Simulation results.

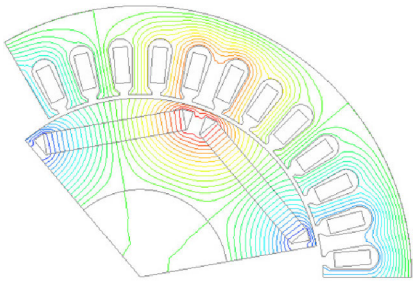

FIGURE 8. The magnetic line of prototype under PMF.

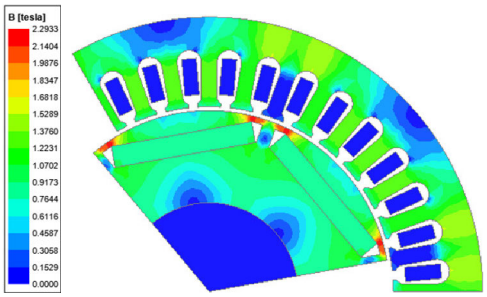

FIGURE 9. The magnetic density map of prototype under PMF.

series connection of both the MMF F_{PM} and the reluctance R_{PM}. Φ_{PM} is the flux excited by the PMs. The air-gap is represented by the reluctance R_{air}, and the core is considered as a flux path without reluctance. Therefore, the influence of the salient effect on the PMF is mainly the additional magnetic resistance caused by PMs buried in the rotor core.

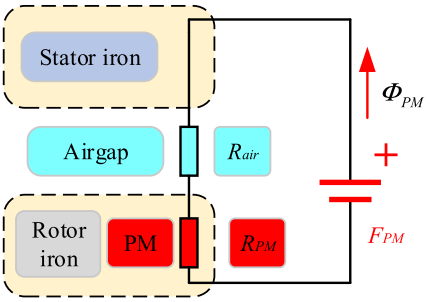

FIGURE 10. The equivalent magnetic circuit of prototype under PMF.

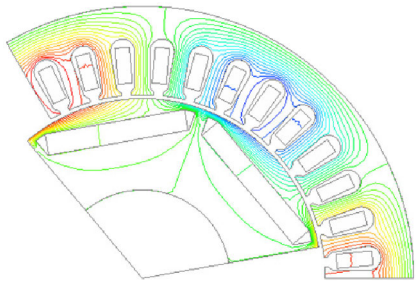

FIGURE 11. The magnetic line of prototype under ARMF.

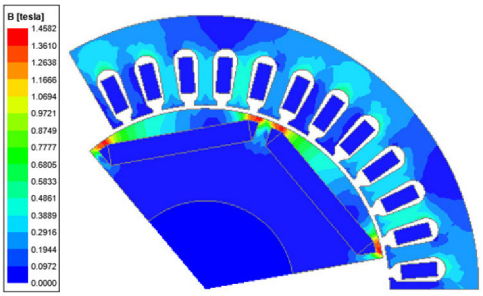

FIGURE 12. The magnetic density map of prototype under ARMF.

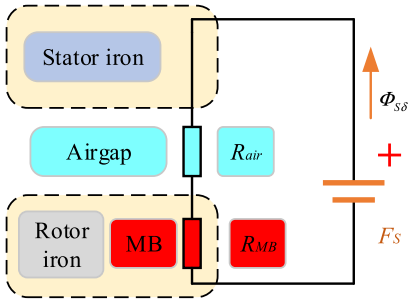

FIGURE 13. The equivalent magnetic circuit of prototype under ARMF.

(ii) Fig. 11 and Fig. 12 show the magnetic field line diagram and magnetic density map of the prototype respectively, when the rated current, containing quadrature- axis and direct-axis components, is given and PMs are replaced with a non-magnetic material. The result shows that the main magnetic field passes through stator core, air gap and

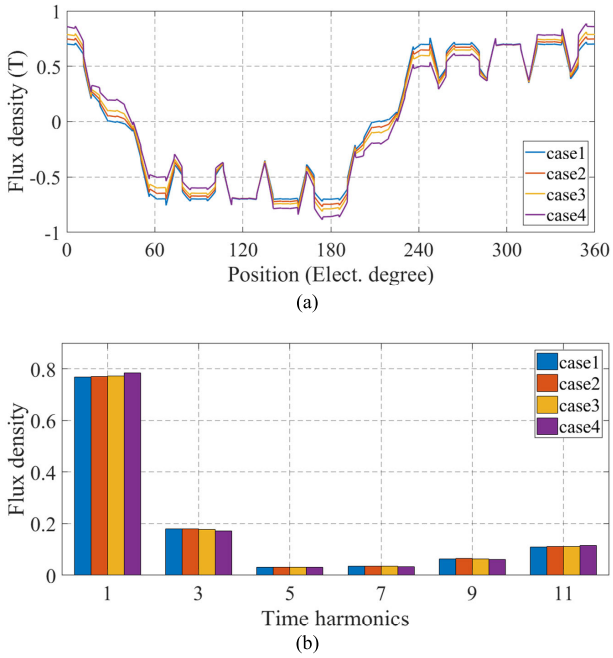

FIGURE 14. The air-gap flux density curves and their FFT results of case 1-4. (a) Flux density curves, (b) FFT results.

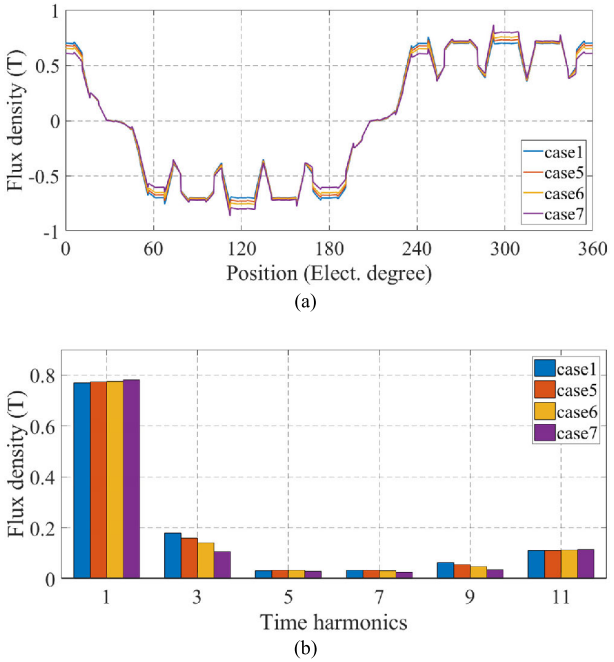

FIGURE 15. The air-gap flux density curves and their FFT results of case 1, and case 5-7. (a) Flux density curves, (b) FFT results.

rotor core, and the rotor core is saturated at the magnetic bridge. Considering the effect of saturation of the rotor core, the model of equivalent magnetic circuit under the action of ARMF is shown in Fig. 13. The influence of the salient effect on ARMF is mainly that the additional magnetic resistance caused by the saturation effect of the magnetic bridge results in the air-gap magnetic field to be distorted.

C. INFLUENCE OF SALIENT EFFECT ON AIR-GAP MAGNETIC FIELD UNDER DIFFERENT CURRENT EXCITATIONS

Table 5 shows seven cases with quadrature-axis current from 0 to I_{qN}, and direct-axis current from 0 to I_{dN}, where I_{qN} and I_{dN} are the rated quadrature-axis current and rated direct-axis current, respectively.

TABLE 5. Current excitation setting of the case 1-7.

Cases	Quadrature-axis current	Direct-axis current
Case1	0	0
Case2	$0.25I_{qN}$	0
Case3	$0.5I_{qN}$	0
Case4	I_{qN}	0
Case5	0	$0.25I_{dN}$
Case6	0	$0.5I_{dN}$
Case7	0	I_{dN}

Fig. 14 shows the air-gap flux density curves and the corresponding FFT results of the case1-4. It can be seen from Fig. 14 (a) that the quadrature-axis current causes the air-gap magnetic field to be distorted, and the distortion becomes more serious as the current increases. According to Fig. 14 (b), the first and third harmonics have obvious change. When the current value is less than $0.5I_{qN}$, the amplitudes of the first and third harmonics remain almost unchanged. When

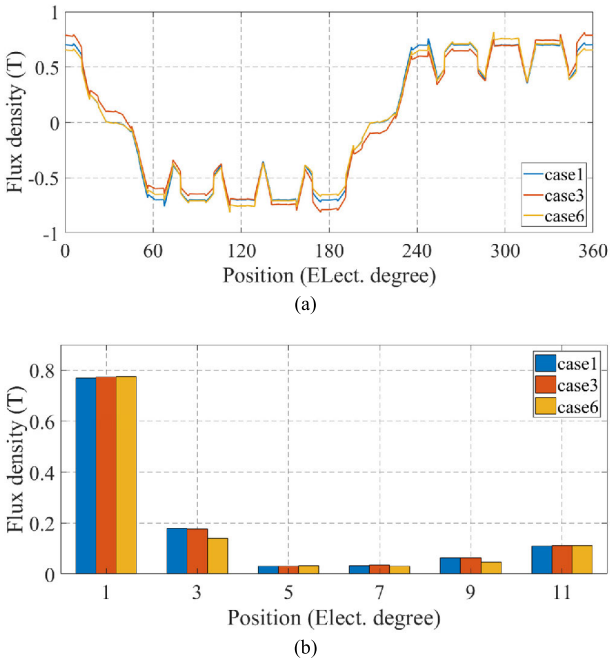

FIGURE 16. The air-gap flux density curves and their FFT results of case 1, 3, 6. (a) Flux density curves, (b) FFT results.

the current value reaches $0.5I_{qN}$, the amplitude of the first harmonic increases, and the amplitude of the third harmonic decreases. In other words, when the quadrature-axis current is large enough, the salient effect will have an impact on quadrature-axis ARMF.

Fig. 15 shows the air-gap flux density curves and the corresponding FFT results of the case1 and case 5-7. It can be seen from Fig. 15 (a) that the direct-axis current has a weak

magnetic effect, and the weak magnetic effect increases as the current increases. According to Fig. 15 (b), the third and ninth harmonics have significant changes, the amplitudes of which decrease as the current increases. Even when the direct-axis current is $0.25I_{dN}$, the salient effect still has an effect on the direct-axis ARMF, which is significantly different from quadrature-axis ARMF.

Fig. 16 shows the air-gap flux density curves and the corresponding FFT results of case1, case3, and case6, respectively. It can be seen from Fig. 14 that the third harmonic of case6 is smaller than that of case3. In other words, compared with the quadrature-axis ARMF, the salient effect has a greater impact on the direct-axis ARMF.

VI. CONCLUSION

In this paper, taking a 6-poles 36-slots IPMSM as an example, the influence of the salient effect on the PMF, ARMF is analyzed. Based on the salient effect function, the spatial-temporal distribution characteristics of PMF and ARMF are investigated, respectively, which are verified by FEM. Then, the prototype experiment is carried out, the measured results are in good agreement with those of the FEM results. Finally, the sources of salient effect are found under different magnetic fields and the influence of the salient effect on air-gap flux density under different current excitations is studied. According to above analysis, the following conclusions can be obtained:

(i) When the salient effect is considered, the air gap permeance is the function of position and time, and increases the harmonic permeance with the temporal orders of $2k_S$. In other words, the air gap permeance changes with time and space, which is different from the conventional analysis in the literature.

(ii) Due to the additional magnetic resistance caused by PMs buried in the rotor core, the salient effect mainly changes the amplitude of the original air-gap magnetic field components under PMF.

(iii) Due to the additional magnetic resistance caused by the saturation effect of the magnetic bridge under ARMF, the air gap magnetic density increases the harmonic components with the temporal orders of $3k_a$ ($k_a = 1, 2, 3\ldots$) and the amplitudes of its various harmonics are also changed under the influence of the salient effect, which is of great significance for the analysis of ARMF and precision control of IPMSM.

(iv) Compared with the quadrature-axis ARMF, the salient effect has a greater impact on the direct-axis ARMF. Therefore, when the air-gap flux density and multi-physical field of IPMSM are further analyzed, the quadrature-axis armature reaction and direct-axis armature reaction should be discussed separately.

REFERENCES

[1] A. Messali, M. A. Hamida, M. Ghanes, and M. Koteich, "Estimation procedure based on less filtering and robust tracking for a self-sensing control of IPMSM," *IEEE Trans. Ind. Electron.*, vol. 68, no. 4, pp. 2865–2875, Apr. 2021.

[2] Z. Huang, C. Lin, and J. Xing, "A parameter-independent optimal field-weakening control strategy of IPMSM for electric vehicles over full speed range," *IEEE Trans. Power Electron.*, vol. 36, no. 4, pp. 4659–4671, Apr. 2021.

[3] X.-H. Chang, Y. Liu, and M. Shen, "Resilient control design for lateral motion regulation of intelligent vehicle," *IEEE/ASME Trans. Mechatronics*, vol. 24, no. 6, pp. 2488–2497, Dec. 2019.

[4] X. Chang and Y. Liu, "Robust H_∞ filtering for vehicle sideslip angle with quantization and data dropouts," *IEEE Trans. Veh. Technol.*, vol. 69, no. 10, pp. 10435–10445, Oct. 2020.

[5] S.-H. Lee, I.-J. Yang, W.-H. Kim, and I.-S. Jang, "Electromagnetic vibration-prediction process in interior permanent magnet synchronous motors using an air gap relative permeance formula," *IEEE Access*, vol. 9, pp. 29270–29278, 2021.

[6] M. M. Ghahfarokhi, E. Amiri, S. T. Boroujeni, and A. D. Aliabad, "On-load analytical modeling of slotted interior magnet synchronous machines using magnetic islands method," *IEEE Access*, vol. 8, pp. 95360–95367, 2020.

[7] J. Wei, D. Yi, X. Bo, C. Guangyu, and Z. Dean, "Adaptive variable parameter impedance control for apple harvesting robot compliant picking," *Complexity*, vol. 2020, Apr. 2020, Art. no. 4812657.

[8] Z. Q. Zhu, D. Howe, E. Bolte, and B. Ackermann, "Instantaneous magnetic field distribution in brushless permanent magnet DC motors. I. Open-circuit field," *IEEE Trans. Magn.*, vol. 29, no. 1, pp. 124–135, Jan. 1993.

[9] Z. Q. Zhu and D. Howe, "Instantaneous magnetic field distribution in brushless permanent magnet DC motors. II. Armature-reaction field," *IEEE Trans. Magn.*, vol. 29, no. 1, pp. 136–142, Jan. 1993.

[10] Z. Q. Zhu and D. Howe, "Instantaneous magnetic field distribution in brushless permanent magnet DC motors. III. Effect of stator slotting," *IEEE Trans. Magn.*, vol. 29, no. 1, pp. 143–151, Jan. 1993.

[11] Z. Q. Zhu, D. Howe, and C. C. Chan, "Improved analytical model for predicting the magnetic field distribution in brushless permanent-magnet machines," *IEEE Trans. Magn.*, vol. 38, no. 1, pp. 229–238, Jan. 2002.

[12] C. Ma, Q. Li, H. Lu, Y. Liu, and H. Gao, "Analytical model for armature reaction of outer rotor brushless permanent magnet DC motor," *IET Electr. Power Appl.*, vol. 12, no. 5, pp. 651–657, May 2018.

[13] X. Zhang, C. Zhang, J. Yu, P. Du, and L. Li, "Analytical model of magnetic field of a permanent magnet synchronous motor with a trapezoidal Halbach permanent magnet array," *IEEE Trans. Magn.*, vol. 55, no. 7, Jul. 2019, Art. no. 8105205.

[14] Z. Li, S. Z. Jiang, Z. Q. Zhu, and C. C. Chan, "Analytical modeling of open-circuit air-gap field distributions in multisegment and multilayer interior permanent-magnet machines," *IEEE Trans. Magn.*, vol. 45, no. 8, pp. 3121–3131, Aug. 2009.

[15] C. Mi, M. Filippa, W. Liu, and R. Ma, "Analytical method for predicting the air-gap flux of interior-type permanent-magnet machines," *IEEE Trans. Magn.*, vol. 40, no. 1, pp. 50–58, Jan. 2004.

[16] H. Kim and J. Moon, "Improved rotor structures for increasing flux per pole of permanent magnet synchronous motor," *IET Electr. Power Appl.*, vol. 12, no. 3, pp. 415–422, Mar. 2018.

[17] H. Chen, D. Li, R. Qu, Z. Zhu, and J. Li, "An improved analytical model for inductance calculation of interior permanent magnet machines," *IEEE Trans. Magn.*, vol. 50, no. 6, Jun. 2014, Art. no. 7027108.

[18] G. Dajaku and D. Gerling, "Stator slotting effect on the magnetic field distribution of salient pole synchronous permanent-magnet machines," *IEEE Trans. Magn.*, vol. 46, no. 9, pp. 3676–3683, Sep. 2010.

[19] Q. Li, T. Fan, and X. Wen, "Armature-reaction magnetic field analysis for interior permanent magnet motor based on winding function theory," *IEEE Trans. Magn.*, vol. 49, no. 3, pp. 1193–1201, Mar. 2013.

[20] D.-K. Lim, K.-P. Yi, D.-K. Woo, H.-K. Yeo, J.-S. Ro, C.-G. Lee, and H.-K. Jung, "Analysis and design of a multi-layered and multi-segmented interior permanent magnet motor by using an analytic method," *IEEE Trans. Magn.*, vol. 50, no. 6, Jun. 2014, Art. no. 8201308.

[21] M. Farshadnia, M. A. M. Cheema, R. Dutta, and J. E. Fletcher, "Analytical modeling of armature reaction air-gap flux density considering the non-homogeneously saturated rotor in a fractional-slot concentrated-wound IPM machine," *IEEE Trans. Magn.*, vol. 53, no. 2, Feb. 2017, Art. no. 8200412.

[22] M. S. Mirazimi and A. Kiyoumarsi, "Magnetic field analysis of multi-flux-barrier interior permanent-magnet motors through conformal mapping," *IEEE Trans. Magn.*, vol. 53, no. 12, Dec. 2017, Art. no. 7002512.

[23] Z. Wu, S. Zuo, S. Hu, and X. Hu, "Analytical modelling of air-gap magnetic field of interior permanent magnet synchronous motors," *IET Electr. Power Appl.*, vol. 14, no. 11, pp. 2101–2110, Nov. 2020.

[24] C. Ma, Y. An, H. Zhao, S. Guo, X. Yin, and H. Lu, "3-D analytical model and direct measurement method of ultra-thin open-circuit air-gap field of interior permanent magnet synchronous motor with multi-segmented skew poles and multi-layered flat wire windings for electric vehicle," *IEEE Trans. Energy Convers.*, vol. 35, no. 3, pp. 1316–1326, Sep. 2020.
[25] L. Xu, W. Zhao, M. Wu, and J. Ji, "Investigation of slot–pole combination of dual-permanent-magnet-excited Vernier machines by using air-gap field modulation theory," *IEEE Trans. Transport. Electrific.*, vol. 5, no. 4, pp. 1360–1369, Dec. 2019.
[26] S. Wang, J. Hong, Y. Sun, and H. Cao, "Analysis of zeroth-mode slot frequency vibration of integer slot permanent-magnet synchronous motors," *IEEE Trans. Ind. Electron.*, vol. 67, no. 4, pp. 2954–2964, Apr. 2020.
[27] L. Zhang, C. Gao, J. Zhang, and X. Wen, "Electromagnetic Vibration Characteristics of PMSMs with Salient Effect," *Trans. China Electrotech. Soc.*, vol. 27, no. 11, pp. 89–96, Nov. 2012.
[28] S. Wang, J. Hong, Y. Sun, Z. Zheng, and H. Cao, "Filling force valley with interpoles for pole-frequency vibration reduction in surface-mounted PM synchronous machines," *IEEE Trans. Ind. Electron.*, vol. 67, no. 8, pp. 6709–6720, Aug. 2020.
[29] X. Wang, X. Sun, and P. Gao, "Study on the effects of rotor-step skewing on the vibration and noise of a PMSM for electric vehicles," *IET Electr. Power Appl.*, vol. 14, no. 1, pp. 131–138, Jan. 2020.

JIAKUAN XIA received the B.S., M.S., and Ph.D. degrees in electrical engineering from the Shenyang University of Technology, China, in 1986, 1997, and 2006, respectively. He is currently a Professor with the School of Electrical Engineering, Shenyang University of Technology. His research interests include modern motion control, power electronics and power transmission, design and research of large synchronous motor excitation systems, and design and control of special motor.

ZEXING LI received the B.S. degree in electrical automatization from the Shenyang University of Technology, Shenyang, China, in 2017, where he is currently pursuing the joint M.S. and Ph.D. degree with the School of Electrical Engineering. His research interests include analysis and suppression of the vibration and noise of the permanent magnetic motors.

ZIXUAN ZHANG received the B.S. degree from the School of Electrical Engineering, Shenyang University of Technology, Shenyang, China, in 2018, where she is currently pursuing the master's degree. Her current research interests include the design and control of permanent magnetic motors.

ZHIYAN GUO received the B.S. degree in electrical automatization from Nanchang University, Nanchang, China, in 2007, and the M.S. degree in electrical engineering from Northeast University, Shenyang, China, in 2014. He is currently pursuing the Ph.D. degree with the School of Electrical Engineering, Shenyang University of Technology, China. His research interests include high-precision servo system in machine tool, vibration abatement, and motion control systems.